Mid-infrared imaging of Supernova 1987A

Mikako Matsuura [1][*] Roger Wesson [1,2] Richard G. Arendt [3,4] Eli Dwek,[3] James M. De Buizer,[5] John Danziger,[6] Patrice Bouchet,[7,8] M. J. Barlow [2] Phil Cigan,[9] Haley L. Gomez,[1] Jeonghee Rho[10] and Margaret Meixner[11,12]

[1]*School of Physics and Astronomy, Cardiff University, Queen's Buildings, The Parade, Cardiff CF24 3AA, UK*
[2]*Department of Physics and Astronomy, University College London (UCL), Gower Street, London WC1E 6BT, UK*
[3]*Observational Cosmology Lab, Code 665, NASA Goddard Space Flight Center, Greenbelt, MD 20771, USA*
[4]*University of Maryland-Baltimore County, Baltimore, MD 21250, USA*
[5]*SOFIA-USRA, NASA Ames Research Center, MS 232-12 Moffett Field, CA 94035, USA*
[6]*Osservatorio Astronomico di Trieste, Via Tiepolo 11, 34131 Trieste TS, Italy*
[7]*DRF/IRFU/DAp, CEA-Saclay, F-91191 Gif-sur-Yvette, France*
[8]*CNRS/AIM, Paris-Saclay University, 91191, France*
[9]*Department of Physics and Astronomy, George Mason University, 4400 University Dr Fairfax, VA 22030-4444, USA*
[10]*SETI Institute, 189 N. Bernardo Avenue, Mountain View, CA 94043, USA*
[11]*Space Telescope Science Institute, 3700 San Martin Drive, Baltimore, MD 21218, USA*
[12]*Department of Physics and Astronomy, The Johns Hopkins University, 366 Bloomberg Center, 3400 N. Charles Street, Baltimore, MD 21218, USA*

ABSTRACT

At a distance of 50 kpc, Supernova 1987A is an ideal target to study how a young supernova (SN) evolves in time. Its equatorial ring, filled with material expelled from the progenitor star about 20 000 yr ago, has been engulfed with SN blast waves. Shocks heat dust grains in the ring, emitting their energy at mid-infrared (IR) wavelengths We present ground-based 10–18 μm monitoring of the ring of SN 1987A from day 6067 to 12814 at a resolution of 0.5 arcsec, together with *SOFIA* photometry at 10–30 μm. The IR images in the 2000's (day 6067–7242) showed that the shocks first began brightening the east side of the ring. Later, our mid-IR images from 2017 to 2022 (day 10952–12714) show that dust emission is now fading in the east, while it has brightened on the west side of the ring. Because dust grains are heated in the shocked plasma, which can emit X-rays, the IR and X-ray brightness ratio represent shock diagnostics. Until 2007 the IR to X-ray brightness ratio remained constant over time, and during this time shocks seemed to be largely influencing the east side of the ring. However, since then, the IR to X-ray ratio has been declining, due to increased X-ray brightness. Whether the declining IR brightness is because of dust grains being destroyed or being cooled in the post-shock regions will require more detailed modelling.

Key words: (stars:) supernovae: individual: Supernova 1987A – ISM: supernova remnants – ISM: dust – (stars:) circumstellar matter – infrared: stars – infrared: ISM.

1 INTRODUCTION

Supernovae (SNe) play a dual role in the evolution of interstellar dust. On one hand, they are the most important source of dust production in galaxies, but on the other had had also the most important source of grain destruction. Theoretical models show that most of the heavy elements produced can precipitate out of the gas and form refractory grains (Sarangi & Cherchneff 2013, 2015; Sluder, Milosavljević & Montgomery 2018; Sarangi, Matsuura & Micelotta 2019). Infrared and submilimetre observations of Cassiopeia A (Barlow et al. 2010; Arendt et al. 2014; De Looze et al. 2017), SN 1987A (Matsuura et al. 2011; Indebetouw et al. 2014; Matsuura et al. 2015), Crab Nebula (Gomez et al. 2012), and young Galactic (up to ∼2000 yr old) SN remnants (Chawner et al. 2019) confirm the presence of ∼0.1–1.0 $M_\odot$

of dust, indicating that a substantial fraction of refractory elements in their ejecta went to dust grains. If the majority of dust in SNe can survive the shock interactions, SNe could be an important source of dust production in the ISM (Dwek & Cherchneff 2011). The fate of this newly-formed dust is still a subject of active studies. The reverse shock traveling through the ejecta can destroy newly-formed dust (Dwek, Foster & Vancura 1996; Schneider, Ferrara & Salvaterra 2004; Nozawa et al. 2007; Biscaro & Cherchneff 2014, 2016; Silvia, Smith & Shull 2010; Micelotta, Dwek & Slavin 2016; Kirchschlager et al. 2019). Any grains surviving the reverse shock may also be destroyed during the injection phase into the interstellar medium (ISM; Slavin et al. 2020) Thereafter, ISM dust will be subject to destruction as it encounters the SN remnant shocks. The grain destruction efficiency and ISM dust lifetimes are highly uncertain since they depend on a long list of parameters. Macroscopic parameters include the energy of the SN explosion, the morphology of the medium surrounding the SN (Slavin et al. 2020), and that of the

[*] E-mail: matsuuram@cardiff.ac.uk

general ISM. Microscopic parameters include the composition and size distribution of the SN condensates, and the detailed interaction of the dust with the shocked gas and other grains (Dwek & Arendt 1992; Jones, Tielens & Hollenbach 1996; Slavin, Dwek & Jones 2015; Kirchschlager, Mattsson & Gent 2021; Priestley, Chawner & of 2021). Because the evolution of dust in the ISM is a fine balance between dust production and destruction, intense investigations are currently underway into dust production and destruction by SNe. In this paper, we examine the latter point of view, and investigate how dust grains are impacted by SN shocks over time.

At a distance of only 50 kpc, SN 1987A provides a unique opportunity for many discoveries, and has been monitored at almost all wavelengths as the SN remnant (SNR) has evolved over the past 30 yr (McCray 1993; McCray & Fransson 2016). The *Hubble Space Telescope* (*HST*) optical images showed that the SN remnant is composed of ejecta and the circumstellar rings (Fig. 1; e.g. Fransson et al. 2015; Larsson et al. 2016; Kangas et al. 2021). The circumstellar rings, which are made of the equatorial ring and the outer rings, consist of the material lost from the progenitor SK −69 202, when the star was in the red-supergiant phase about 20 000 yr ago (McCray 1993). Eventually, the merger of a $\sim$15 M$_\odot$ and a $\sim$5 M$_\odot$ binary (Morris & Podsiadlowski 2007) created a blue-supergiant, and the circumstellar ring had been polluted by the material from faster but thinner wind from the blue supergiant. The outer ejecta, which were expelled by the SN explosion and are mainly composed of hydrogen and helium, expand at 2 000–10 000 km s^{-1} (Larsson et al. 2016; Kangas et al. 2021). The equatorial ring expands much slowly ($\sim$100 km s^{-1}; Larsson et al. 2019), and has been caught up by the outer ejecta, experiencing shocks.

The equatorial ring, hereafter the ring, in SN 1987A provides an excellent place to study dust grains undergoing shocks. Combined X-ray and infrared (IR) observations can provide important information of the interaction between dust grains and the shocked X-ray emitting gas (Dwek et al. 2010). Mid-IR observations of SN 1987A have shown the presence of hot, $\sim$180 K, silicate dust (Dwek 1987; Bouchet et al. 2004, 2006; Dwek et al. 2008), presumably collisionally heated by the shocked gas. The plasma that heats the dust and gives rise to the X-ray emission also destroys the dust that is swept up by the SN shock.

In this paper, we present mid-IR monitoring from day 6067–12814 of the ring images at a resolution of $\sim$0.5 arcsec. These details allow us to follow the simultaneous evolution of the X-ray and IR emission of the different sections of the ring over time. These images and fluxes are compared with collisionally heated dust models, whose global parameters have been constrained by X-ray measurements of the plasma conditions.

2 OBSERVATIONS

2.1 VLT/VISIR observations in 2017, 2018, and 2022

The VLT Spectrometer and Imager for the mid-InfraRed (VISIR; Lagage et al. 2004; Käufl et al. 2015) obtained images of SN 1987A, under the program 298.D-5023(A). The images of SN 1987A were taken around the 30 yr anniversary mark on 2017 February 15 (day 10 950 since the explosion), February 17 (day 10 952), and March 13 (day 10 976). All were obtained with the B10.7 (10.7 μm) filter. The seeing was typically in the range of 0.3–0.5 arcsec (full width at half-maximum; FWHM) in the mid-infrared, according to observations of calibration stars. The airmass was between 1.41 and 1.56. The pixel scale is 0.04 arcsec, using regular imaging mode, with a field of view of 38 × 38 arcsec^2. The standard chop-nod technique was

used to subtract sky and instrumental backgrounds, with chopping frequency of 3.99 Hz, while the nodding was east-to-west parallel to the chopping direction. The amplitude of both the chop and nod throws was 8 arcsec. Although VISIR can offer jittering mode, we used non-jittering mode, in order to avoid difficulty in stacking jittered frames. The total integration time was 6450 s on source. Six stars (HD41047, HD49968, HD35536, HD39523, HD47667, and HD32820) were used for flux calibration, and their fluxes were estimated from Cohen et al. (1999)'s flux calibration list. The data on February 15 and 17 were taken during clear conditions with high humidity ($>$ 50 per cent), thus flux density measurements from those nights seem to suffer from larger uncertainties.

VISIR also obtained Q1 (17.65 μm) images, with program IDs of 298.D-5023(A) and 0102.D-0245(A) in 2017 and 2018. The optical seeing was 0.4–1.5 arcsec, typically, occasionally reaching 2.0 arcsec. Unless the mid-infrared seeing is really poor, *Q*-band angular resolution is determined by the 8.2-m telescope's diffraction limit of 0.54 arcsec (the diameter of the first ring with 'null' signal; Reunanen, Prieto & Siebenmorgen 2010), unlike the normally seeing-limited resolution at *N*-band. Indeed, the FWHM of the photometric calibration source was recorded as 0.4–0.5 arcsec. The airmass was 1.40–1.48. We measure the total flux of these Q1 images for 2017 and 2018, separately, but for our figures in this paper, we combined the data from these 2 yr, in order to increase the image quality. The pixel scale, field of view and chop-nod settings were the same for B10.7 observations. There were in total eight observing blocks, and data from five of these were used, as the remaining three had poor quality. That resulted in the total integration time of 11 250 s on source. Five flux calibration stars (HD39523, HD22663, HD41047 HD23319, and HD28413) were used.

4 yr later, VISIR revisited SN 1987A, imaging in the B10.7 band in 2022 January and March under the program 106.D-2177. The images were taken at three separate days, 2022 January 31 (day 12 760), 2022 March 1 (day 12 789) and 2022 March 26 (day 12 814). The optical seeing varied between 0.4–2.2 arcsec on January 31, whereas it was slightly better on other 2 d (0.45–1.73 arcsec on March 1, and 0.4–1.8 arcsec on March 26). Five different calibration sources were used on January 31 (HD026967, HD035536, HD082660, HD041047, and HD083425), while on March 1, HD041047 and HD055865 were used, and HD112213 and HD114326 on March 26. The total integration time was 10 900 s on source.

All the VISIR data were reduced, using ESO reduction package, ESOREFLEX (Freudling et al. 2013). The final images were smoothed with a 2-pixel Gaussian filter, in order to increase the signal to noise ratio.

Fig. 1 includes VISIR images of SN 1987A taken in the B10.7 in 2017 and in 2022. Fig. 2 shows a Q1 band VISIR image of SN 1987A taken in 2017 and 2018. These images clearly show MIR emission from the ring, with the brightest areas being on the south-west side of the ring. In the B10.7 band, individual clumps within the ring are marginally resolved.

Bouchet et al. (2004) reported an unresolved central source in their 10 μm image in 2003 (also seen in Fig. 1). That source was not detected in the subsequent 11 μm image in 2005 (Bouchet et al. 2006). There is a potential point source at the centre of the ring in 10.65 μm image in 2017 and 2022 (Fig. 1). Whether this point source is a real detection or not is unclear, as it is close to the noise level, generated by imperfect reconstruction of the point spread function. If this point source detection is real, it could be due to ejecta dust (Bouchet et al. 2006), but also related with the compact source (Alp et al. 2018; Page et al. 2020). The definitive existence (or not) of this central point source awaits JWST.
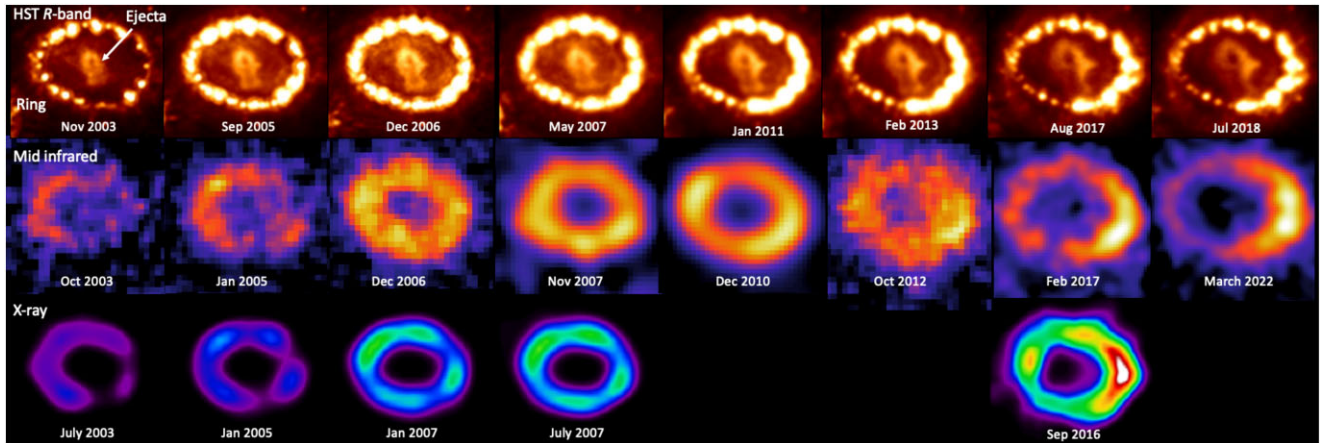
Figure 1. Time evolution of SN 1987A images, showing how the blast waves progress in time. The north is top and the east is left. The north-east side of the ring brightened, in early 2003, and its brightness increased in 2000's, as the blast waves gradually passed with the brightest blobs at the north-east side of the ring. In meanwhile, in 2010's images, the west side of the ring is the brightest. *HST R*-band images are from Larsson et al. (2019), mid-infrared images from Bouchet et al. (2006) and this work, and X-ray 0.3–8 keV images from Frank et al. (2016) and Frank & Burrows (private communication). Note that mid-infrared images were taken with different filters around 10 μm and have large uncertainties in fluxes, hence, the relative brightness at different epochs is not accurate.
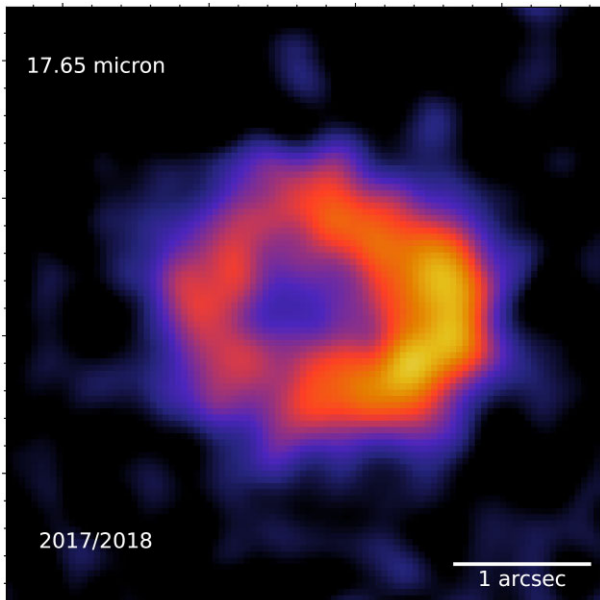
Figure 2. VISIR image of SN 1987A in the Q1 band (17.65 μm), combined from 2017 and 2018 observations.

2.2 SOFIA observations in 2017 and 2019

Following the Cycle 4 observations in 2016 (Matsuura, De Buizer & et al. 2018), the NASA *Stratospheric Observatory For Infrared Astronomy* (*SOFIA*; Young et al. 2012) observed SN 1987A during Cycle 5 in 2017. *SOFIA*'s FORCAST instrument (Herter et al. 2012) obtained photometry during a Southern hemisphere campaign with the aircraft temporarily based in Christchurch, New Zealand. FORCAST is equipped with two cameras, a short wavelength camera, operating at 5–25 μm, and a long wavelength camera, operating at 25–40 μm, both of which have a pixel scale of 0.768 arcsec per pixel. We used the dual channel mode of FORCAST, that employs a dichroic to allow imaging in both cameras simultaneously. Observations of SN 1987A were taken on two separate flights (Flight 426 and 427). On 2017-08-06, FOR_F112 (centred at 11.2 μm) and

FOR_F315 (centred at 31.5 μm) filters were used on Flight 427 on 2017-08-06 (11 122 d since the explosion), while FOR_F197 (centred at 19.7 μm) and FOR_F315 were used for the Flight 426 on the 2017-08-03 (day 11 119). The total exposure times on source were 3181 s for FOR_F112, 2274 s for FOR_F197, 3486 + 2686 s for FOR_F315, respectively. Observations were performed using the 'Nod-Match-Chop' mode, i.e. the same method employed by the VLT for the VISIR observations mentioned earlier, and were configured to have 45 arcsec east–west chop and nod throws. Unfortunately, SN 1987A was not detected in the FOR_F112 band.

SOFIA further observed SN 1987A with FORCAST in 2019 on July 1, and July 8–11. Similar to previous flights, 'Nod-Match-Chop' mode was used. During these flights (Flight 588 and 592–595), FOR_F197 and FOR_F315 were observed separately, without the dichroic. The total exposure time was 15016 s for FOR_F197 and 16070 s for FOR_F315.

2.3 Archival data

SN 1987A was monitored in the mid-infrared by Gemini-South/T-ReCS (Li, Telesco & Varosi 2010) and the observations up to 2003 have been reported by Bouchet et al. (2006). Fluxes in Table 1 are taken from Bouchet et al. (2006). Further images were taken by Gemini-South T-ReCS and VLT/VISIR from 2005 to 2012, and their fluxes are also listed in Table 1. VISIR underwent detector upgrade in mid 2010's, and the VISIR images taken in 2007 and 2010 before this upgrade had a pixel scale of 0.075 arcsec.

SOFIA observed SN 1987A with *FORCAST* in 2016, and the fluxes are taken from Matsuura et al. (2018).

3 RESULTS

3.1 Time evolution in the mid-infrared images with comparison to optical and X-ray images

The *Hubble Space Telescope* (*HST*) *R*-band images in Fig. 1, taken from Larsson et al. (2019), demonstrate the structures and evolution of the remnant of SN 1987A. The bright ring, which is often called the 'inner ring' or 'equatorial ring', is one of the circumstellar rings

Table 1. Observing log.

Telescope/instrument	Program ID	Date	Day	Filter	λ_{eff}	$\Delta\lambda$	Flux (mJy)
Gemini-South/T-ReCS		2003-10-04	6067	N	10.36	2.89	9.9 ± 1.5
Gemini-South/T-ReCS		2005-01-07	6526	Si-5	11.66	1.13	18.4 ± 1.2
Gemini-South/T-ReCS		2005-02-01	6552	Qa	18.30	1.51	53.4 ± 9.0
Gemini-South/T-ReCS	GS-2004A-Q-3	2005-11-04	7194	Si-5	11.66	1.13	20 ± 2
Gemini-South/T-ReCS	GS-2006B-Q-3	2006-12-22	7242	N	10.36	2.89	19 ± 2
VLT/VISIR	080.D-0105	2007-10-07	7533	PAH2	11.88	0.37	48 ± 7
VLT/VISIR	086.D-0192	2010-12-27	8708	B10.7	10.65	1.37	35 ± 6
Gemini-South/T-ReCS	GS-2012B-Q-90	2012-10-25	9376	N	10.36	2.89	38 ± 4
SOFIA/FORCAST	04_0016	2016-07-11	10732	FOR_F111	11.2	2.7	45 ± 7
				FOR_F197	19.7	5.5	88 ± 9
				FOR_F315	31.5	5.7	105 ± 14
VLT/VISIR	298.D-5023	2017-02-15 & 02-17 & 03-13	10952–10976	B10.7	10.65	1.37	(26) ± (5)
		2017-09-13	11160–11181	Q1	17.65	0.83	114 ± 40
SOFIA/FORCAST	05_0050	2017-08-03	11119	FOR_F197	19.7	5.5	82 ± 11
				FOR_F315	31.5	5.7	113 ± 19
VLT/VISIR	102.D-0245	2018-12-03	11606–11611	Q1	17.65	0.83	128 ± 16
SOFIA/FORCAST	07_0064	2019-07-11	11826	FOR_F197	19.7	5.5	104 ± 9
				FOR_F315	31.5	5.7	76 ± 15
VLT/VISIR	106.D-2177	2022-01-31 & 03-01 & 03-26	12760–12814	B10.7	10.65	1.37	42 ± 13

found in SN 1987A, with the other ring being fainter and farther (up to ∼5 arcsec in diameter) 'outer rings' (Panagia et al. 1996). The inner ring is composed of about 20 clumps within, while the ejecta appear as a central keyhole-shaped cloud, expanding in time.

3.1.1 Evolution of brightness distribution within the ring

The *HST* monitoring program observed that as the ejecta expanded, the ring brightened until ∼2011, and then began getting fainter (Fig. 1; Fransson et al. 2015). At *R*-band, in 2003 the ring was relatively faint, and gradually increased its brightness in time. The ring was brightest at the north-east and south-west (Fransson et al. 2015). In 2005 (day ∼7000), some of the knots in the north-east side of the ring started fading (Fransson et al. 2015; Larsson et al. 2019). The peak brightness shifted from the east to the west side of the ring in 2006 (Fransson et al. 2015; Larsson et al. 2019). The brightness on the west side continued to increase till 2011, and then started fading too (Larsson et al. 2019).

The second row of Fig. 1 shows the mid-IR (mid-IR) time evolution of SN 1987A images. The time evolution at MIR wavelengths follows more or less similar trends to the ring evolution in *HST* images. Initially only the east side of the ring was visible in the 2003 image. As the blast waves progressed, the north-east side of the ring brightened, first in the mid 2000's. Eventually, the brightness of the west side of the ring caught up with the east side in 2007, and in 2017 the west side of the ring is the brightest.

In the X-ray, *Chandra* images at 0.3–8 keV show that the east side of the ring was bright until 2007 (day ∼7000) (Frank et al. 2016). Since 2009, the west side of the ring is dominating the brightness. Unlike *HST* images, the total brightness at X-ray wavelengths continued to increase until 2009 (day ∼9000). In the 0.5–8 keV and 0.5–2 keV bands, the total brightness plateaued, while the 3–8 keV brightness continued to increase beyond 2009 (Frank et al. 2016).

Fig. 3 shows the time evolution of east-west ratio of the emission within the ring at 10–12 µm. The diagram follows the fraction of the emission coming from the east side of the ring, with respect to
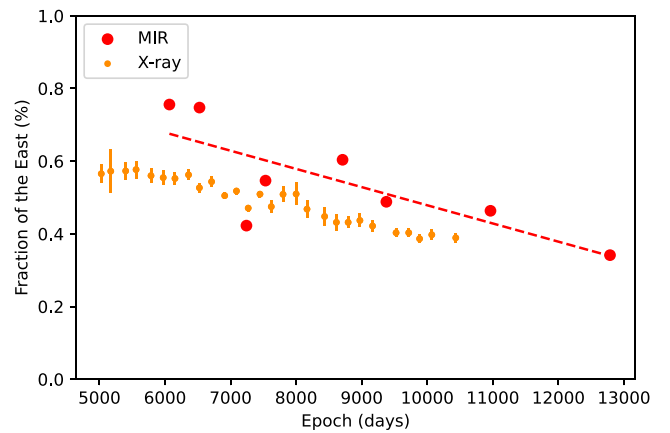
Figure 3. The fraction of the MIR emission originating from the east half of the ring with respect to the total emission at 10–12 µm. The dashed line is a linear fit to the measured fractions. The time variation of the fraction in X-ray (Frank et al. 2016) is also plotted. Both X-ray and MIR show declining trend in the fraction emitted from the east half, however, the fraction tends to be higher in MIR than X-ray.

the total emission. The uncertainties, estimated by shifting the east-west border by one pixel, were typically less than a few per cent. The ratio taken in 2006 (day 7242) is a low outlier in this figure, and it appears that this data set seems to have suffered from negative backgrounds in the surroundings. The east side of the ring produces nearly 80 per cent of the total brightness in day ∼6000, and this fraction declines in time, down to ∼40 per cent in day 12 800.

Although a general decreasing trend of the east fraction is consistent with that found in X-ray images at 0.3–8 keV (Frank et al. 2016), the actual IR values tend to be higher. Around day ∼6000, the IR fraction from the east was nearly 80 per cent, whereas for X-rays it was only 57 per cent. The fraction dropped to only about 50 per cent at day 10 000, while the X-ray fraction from the east was 38 per cent. The IR emission might have a delayed response time, after the shock hit the ring, traced by X-ray emission.
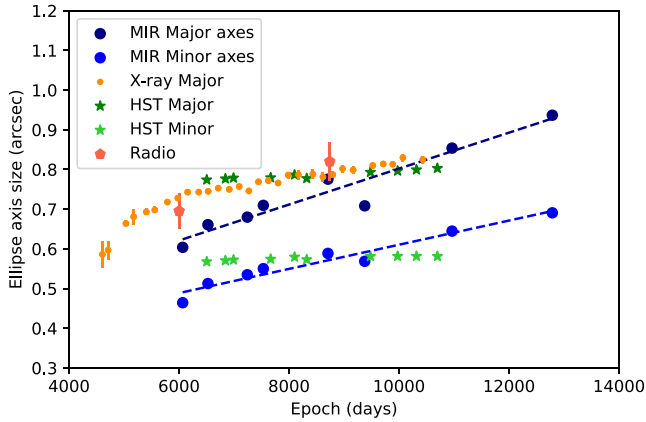
Figure 4. The major and minor axes of ellipse fitting to the 10–12 μm MIR ring images, as a function of time. The ellipse is expanding. As a comparison, X-ray (Frank et al. 2016) *HST* optical ellipse sizes and the 18 GHz synchrotron east-west radii, which are equivalent to the ellipse major axes, from Zanardo et al. (2013), are also plotted. The X-ray size increased initially but flattened recently. The optical size remains almost constant. The radio size seems to follow the X-ray trend.

3.1.2 Size of the ring

Fig. 1 suggests that the mid-infrared diameter of the ring may be slightly larger in 2017 (day 10 952–10 976) and in 2022 (day 12 760–12 814), compared with 2005 (day 7194). Fig. 4 shows that the major and minor axes measured in mid-infrared images are increasing in time. The fitting used 2D Gaussian fitting, utilizing MPFIT2DFUN in IDL (Markwardt 2009). The B10.7-band angular resolutions are limited by the seeing, and the FWHMs of the point-spread functions (PSFs) of the calibration stars were recorded at 0.3–0.5 arcsec in 2017 and 0.3–0.4 arcsec in 2022. Given this angular resolution, the increasing trend over 7000 d is likely to be real. Although we have to be careful about unexpected image distortions, caused by chop-nod observations, the ring seems to expand over time in the MIR images. The lines in Fig. 4 are fits to the measured ellipse sizes, corresponding to expansion at 3920 km s^{-1} for the major axis, and 2636 km s^{-1} at 50 kpc. The inclination angle of the ring was estimated to be 38–45° (Burrows, Kristx & Hester 1995; Larsson et al. 2019), and our measured ratio of major and minor axes is consistent with this inclination angle..

In the optical, there is nearly no expansion found. *HST* images recorded the diameter of the ring could be expanding by merely 0.02–0.04 arcsec between day 7000 and 9000 (Fransson et al. 2015). We measured *HST* ellipse sizes before day 7000 and beyond 9000 (Fig. 4), and even in the longer time span, the size remains almost constant.

On the other hand, the X-ray radius has been reported to have increased from 0.728 to 0.830 arcsec from day 5978 (in 2003) to day 10 073 (in 2014) (Frank et al. 2016), and their measurements are replicated in Fig. 4. These reported X-ray sizes are more or less consistent with the MIR estimates of the major axes, but slightly smaller. The X-ray has provided more frequent measurements, and up to day ∼6500, the expansion of the radius at 0.5–2 keV was fitted by 6711 ± 787 km s^{-1} and later epochs by 1854 ± 101 km s^{-1} (Frank et al. 2016). The MIR expansion rate was 3920 km s^{-1} for the major axis, which was faster than the X-ray 0.5–2 keV band until recently. The higher energy X-ray band at 2–10 keV continues to expand at a higher rate of 3071 ± 299 km s^{-1} (Frank et al. 2016), closer to MIR velocities. The radial expansion velocity was also measured in
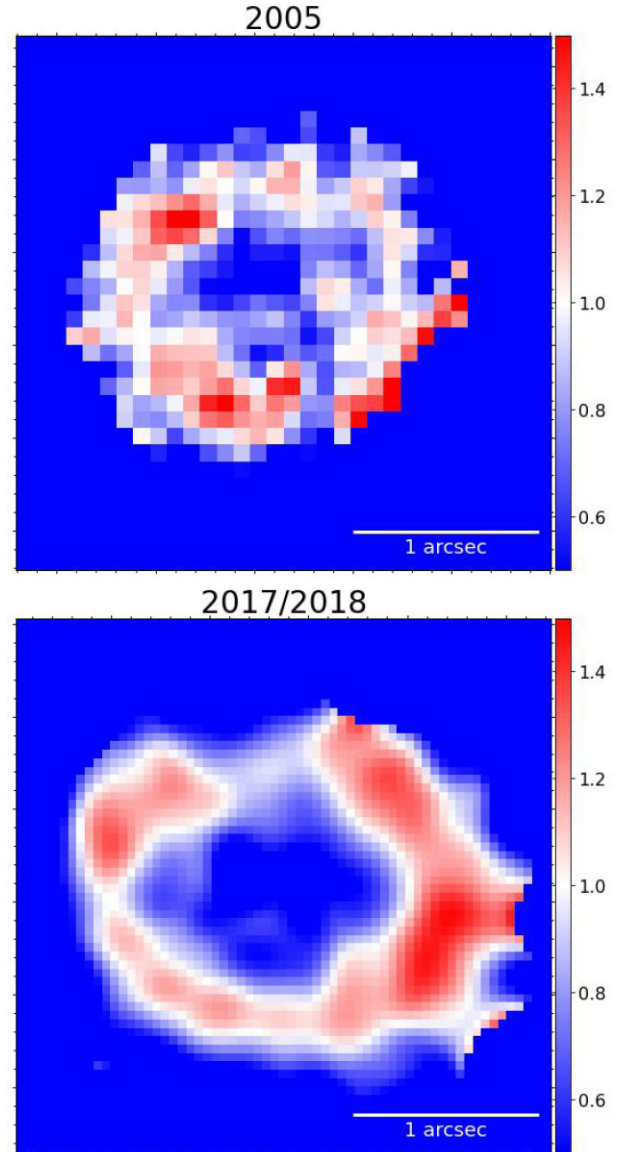
Figure 5. The relative brightness ratios of $I_\nu(\lambda = 11.88)/I_\nu(\lambda = 18.30)$ in 2005 (top) and $I_\nu(\lambda = 10.7)/I_\nu(\lambda = 17.65)$ in 2017 and 2018 (bottom). The ratios are scaled so that the mean values of surface brightnesses become unity. Higher values of ratios, indicating higher dust temperatures within the ring, are found in the north-east in 2005, while they are located in the south-west in 2017/2018.

synchrotron radiation at radio frequencies, and the expansion velocity measured at 9 GHz (Ng et al. 2013; Zanardo et al. 2014) continued to be 3890 ± 50 km s^{-1} (Frank et al. 2016), which is close to the MIR measurement.

3.2 Dust temperature indicator

The ratio of two MIR band images gives a measure of the dust temperature distributions within the ring. Fig. 5 shows the relative brightness (I_ν) ratios of $I_\nu(\lambda = 11.88)/I_\nu(\lambda = 18.30)$ in 2005 (top) and $I_\nu(\lambda = 10.7)/I_\nu(\lambda = 17.65)$ in 2017 and 2018 (bottom). Unfortunately, there was some issue in the absolute flux calibration of $I_\nu(\lambda = 10.7)$ in 2017, so that we have taken the median of the surface brightnesses across the ring, and these ratios indicate excess above/below the median values. Although these ratios are unable to give the actual
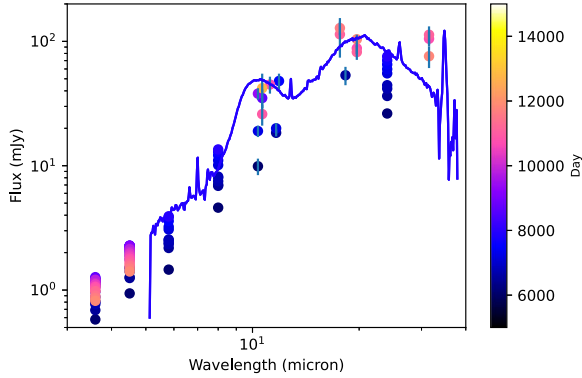
Figure 6. The time evolution of the MIR spectral energy distributions. The colours of the plotted points indicates the dates of observations, shown in the colour-scale bar. The plot includes *Spitzer* IRS 5–28 μm spectrum, with corresponding colour for the date observations.

dust temperatures, they are indicative of warmer and colder dust temperatures within the ring at a given time.

In 2005, the north-east part of the ring shows relatively higher ratios, indicating higher dust temperatures. That is consistent with the location of the brightest part of the ring in the MIR image (Fig. 1). In 2017, the brightest part of the the ring is shifted towards the south-west (Fig. 1), and that part of the ring also has the highest ratio of $I_\nu(\lambda = 10.7)/I_\nu(\lambda = 17.65)$, indicating the highest dust temperature at this location.

Brightness ratio maps show that the shift of brightness peak from north-east to south-west is mainly caused by the change of the dust temperatures. The brightness of MIR dust emission depends on both dust temperature and column density along the line of the site. When it is optically thin ($\tau(\lambda) \ll 1$),[1] the brightness of the dust emission reaches $I_\lambda = \tau_d(\lambda)B_\lambda(\lambda, T_d)$ (Spitzer 1978; Rybicki & Lightman 1986), where $\tau_d(\lambda)$ is the dust optical depth at wavelength λ, and $B_\lambda(\lambda, T_d)$ is the Planck function at the dust temperature T_d (Gordon et al. 2014). The optical depth $\tau_d(\lambda)$ is represented by $\kappa(\lambda)\Sigma_d$, where $\kappa(\lambda)$ is the dust absorption cross-section and Σ_d is the dust surface mass density (Spitzer 1978; Gordon et al. 2014). The ratio of brightnesses at a given time does cancel out Σ_d, hence, this value only depends on T_d. The time variation of relative brightness shift from the east to west (Fig. 1) is influenced by the dust temperature T_d. The T_d was higher in the east in 2005, while it is higher in the west in 2017/2018.

3.3 Time evolution of the MIR spectral energy distributions

Fig. 6 shows the time variation of the spectral energy distributions (SEDs). The colour of the plotting points indicate the observed day since the explosion. The majority of the photometry data points are from *Spitzer Space Telescope* monitoring programs (Dwek et al. 2010; Arendt et al. 2016). These include 3.6, 4.5, 5.8, 8.0, and 24 μm photometric data points, as well as 5–35 μm Spitzer/IRS spectra. The Spitzer/IRS spectrum shows that photometry at ~10 and ~20 μm are strongly affected by the broad silicate features. Although *Spitzer* took spectra at multiple epochs, only the last spectrum at day 7954 is plotted in Fig. 6. *Spitzer* monitoring at 3.6 and 4.5 μm continued after *Spitzer*'s helium coolant was exhausted, showing that

---

[1]The optical depth, calculated from M_d from Section 3.3, with an assumption of the clump thickness of 0.05 arcsec and an ellipse size from Fig. 4 is $\tau_d = 0.002$ at 10 μm, i.e. optically thin on day 10 964.

their fluxes reached a peak at about day 8500–9000 in 2009–2010 (Arendt et al. 2020). Other *Spitzer* bands were last observed on day 7975–7983, just before these bands would have peaked in brightness (Arendt et al. 2020).

All ground-based photometry at 10–12 μm after day 10 000 falls below the day 7954 *Spitzer* spectra. At 18–20 μm and 31.5 μm such a trend is unclear. Within the uncertainties, 18–20 μm fluxes after day 10 000 are more or less comparable to the flux measured by *Spitzer* on day 7954. The *SOFIA* 31.5 μm fluxes are higher than day 7954 *Spitzer* spectra at the same wavelength, as reported by Matsuura et al. (2018).

The brightness ratios of the N- and Q-band images demonstrate the spatial variations of the temperature within the ring (Fig. 5). We evaluate whether these variations may be reflected in the overall SED, by fitting the SED with a modified blackbody, representing the dust emission.

The flux density F_ν with frequency grid ν from a dust mass (M_d) can be characterized by a modified blackbody of the form of

$$F_\nu(\lambda) = M_d \frac{4\kappa(\lambda)\pi B_\nu(\lambda, T_d)}{4\pi D^2}, \tag{1}$$

where M_d is the dust mass, $B_\nu(\lambda, T_d)$ is the Planck function, and T_d is the dust temperature (Hildebrand 1983). This modified blackbody assumes that the dust emission is optically thin. D is the distance to the LMC, adopted to be 50 kpc. $\kappa(\lambda, a)$ is the dust mass absorption coefficient, $\kappa(\lambda, a) = 3Q(\lambda)/4\rho a$, where ρ is the mass density of the dust grains, $Q(\lambda)$ is the dust emissivity at the wavelength λ, and a is the grain size. In this SED fit, we assumed a single grain size of 0.1 μm. This grain size is relatively large within the typical grain size distributions adopted in the ISM (50 Å–0.25 μm; Weingartner & Draine 2001), however, slightly smaller but similar to the past estimate of dust in the ring (>0.2 μm; Dwek et al. 2010). This assumption affects estimated T_d and M_d, but not the total IR luminosity.

First, we fitted the data near the peak of the silicate feature with a single dust component (case 1). Silicate dust emissivity is calculated from Draine & Lee (1984). For day 7954, the Spitzer IRS spectrum from 5 μm to 33 μm was taken into account. For day>10 000, we used all photometry, including *SOFIA* 31.5 μm for case 1.

Case 2 uses two-component fits for hot and warm dust, following Dwek et al. (2010). The warm dust component represents silicate emission around 8–20 μm, similar to case 1. There is an additional emission component to fit *Spitzer* 3.6 and 4.5 μm data points, and that contributes to the underlying emission at longer wavelengths (Dwek et al. 2010). Although the exact nature of this emission component is unknown, we call it 'hot' dust, and fit with amorphous carbon (Zubko et al. 1996). Dwek et al. (2010) fitted this component with alternative dust compositions, such as Fe, Fe_2O_4, FeS, but in this work, we tested only with amorphous carbon, as the exact composition of dust is unknown only with two bands. Although we tried to fit the hot component with silicates, the resultant fit had a far higher χ^2 value, so that we excluded it from further analyses.

There is additionally a cold ejecta dust component, representing far-infrared emission at 70 μm and longer wavelengths (Indebetouw et al. 2014; Matsuura et al. 2015, 2018; Cigan et al. 2019). At the moment, this component is not included in the analysis, because the mid-infrared dust emission is dominated by the ring dust.

Best fitted parameters were searched, using the IDL version of the AMOEBA function (Press et al. 1989), and the uncertainties of parameters were evaluated by Monte Carlo method, using the IDL version of RANDOMN function (Press et al. 1989). Table 2 summarizes
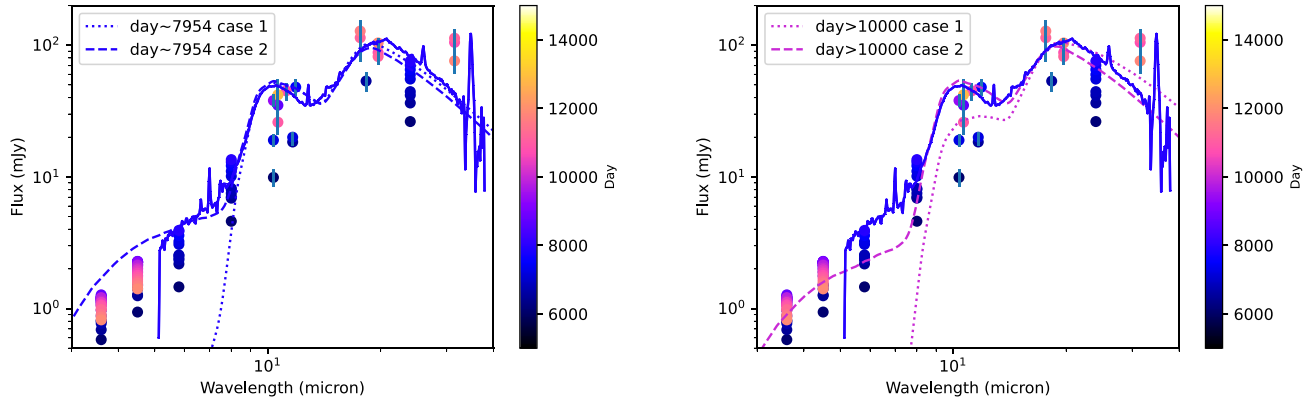
Figure 7. Dust model fittings to the photometry and Spitzer IRS spectra at day ∼7954 (left) and photometry at day ∼10 000 (right). Note that all data points in Fig. 6 are plotted in both panels, so that the time variations can be found. The fitted results have little difference in the flux levels at 10 and 19 μm.

Table 2. The results of modified blackbody fits to the IR SEDs at day ∼7954 and day >10 000. Case 1 is for a single component dust emission and case 2 is for two-component dust emissions.

			Day ∼7954	Day >10 000
Case 1	Data		IRS only	>8 μm only
		Dust	Silicate	Silicate
		M_d ($M_\odot$)	$(1.110 \pm 0.003) \times 10^{-5}$	$(2.6 \pm 1.3) \times 10^{-5}$
		T_d (K)	184.9 ± 0.1	154 ± 5
Case 2	Data		3.5, 4.6, 5.8, 8.0 μm, and IRS	3.6, 4.5 μm, and >8 μm
	Hot	Dust	Amorphous C	Amorphous C
		M_d ($M_\odot$)	$(1.31 \pm 0.07) \times 10^{-8}$	$(0.7 \pm 0.7) \times 10^{-8}$
		T_d (K)	525.6 ± 0.5	525.40 ± 0.09
	Warm	Dust	Silicate	Silicate
		M_d ($M_\odot$)	$(0.90 \pm 0.03) \times 10^{-5}$	$(0.9 \pm 0.3) \times 10^{-5}$
		T_d (K)	190.9 ± 1.0	191.3 ± 0.2

the parameters derived from the fitted results and fitted results are plotted in Fig. 7.

The dust temperatures (T_d) of a single component fit (case 1) suggest that the overall temperature might have dropped from 185.9 ± 0.1 K to 154 ± 5 K from day ∼7954 to day >10 000. The very small uncertainty of ±0.1 K on early days is due to the very small uncertainties of *Spitzer* IRS spectra, which are propagated into the temperature uncertainties. The uncertainties do not include any systematic errors related to the either the flux measurements (e.g. calibration) or the choice of $\kappa(\lambda)$ for the model. However, the warm dust temperatures for a two-component fit (case 2) remain more or less the same. Indeed, the case 2 hot component fit has smaller dust temperature uncertainties at day >10 000 than the day ∼7954 fit, but large dust mass uncertainties, with no constraints, suggesting a shortcoming of our simple fit. Therefore, even though spatially resolved images indicate the change of dust temperature at different parts within the ring, the SED is rather insensitive to these changes, because the SED contains both increasing and decreasing small-scale temperature changes.

3.4 Light curve analysis

Fig. 8 shows light curves at three different wavelengths. The measurements at 31 μm are solely from *SOFIA*, while those at 10–12 μm and 19 μm were collected from different instruments with slightly different filter systems, so that they are not a completely uniform sample. Nevertheless, these light curves generally follow those estimated from *Spitzer* 3.6 and 4.5 μm measurements (Arendt
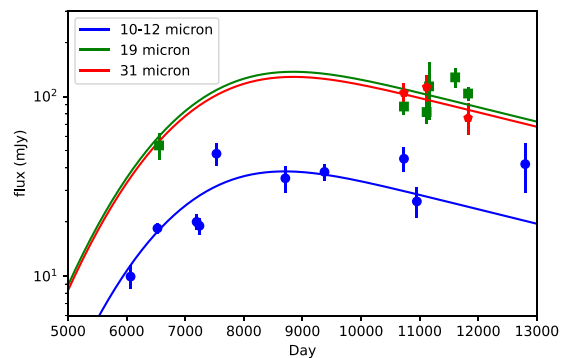
Figure 8. The time evolution of flux densities at 10–12, 19, and 31 μm, assembled from multiple measurements from GEMINI, VLT, and *SOFIA* (Table 1). The light curves, simply scaled from those fitted to the *Spitzer* 8 and 24 μm flux densities, can replicate the flux evolutions very well.

et al. 2020). Arendt et al. (2020) demonstrated that the 3.6 and 4.5 μm light curves are well represented by a convolution of exponential decay and a Gaussian function. These fittings are extended to the 8 and 24 μm *Spitzer* bands, too. The curves in Fig. 8 use the same Gaussian σ and exponential τ parameters as *Spitzer* 8 and 24 μm but the heights are scaled. Surprisingly, the 19 μm fluxes from GEMINI and ESO/VISIR follow the *Spitzer* 24 μm light curve well. The 10–12 μm fluxes follow the scaled *Spitzer* 8 μm light curve, but have a larger scatter. This scatter is most likely because these wavelengths cover the silicate features, and depending on the filter transmissions,

flux can change substantially. The light curves demonstrate that there is very little difference in flux level at day ∼7954 and 10 000, as found in Fig. 7, because the fluxes still increased from day ∼7954, reaching a peak at about day ∼8500, and then decreasing afterwards, coming back to a similar level to that around day ∼7954.

4 DISCUSSION

The IR emission from the ring is produced by dust grains that are collisionally heated by the same gas that also gives rise to the X-ray emission. This creates an intimate connection between the basic physical properties of the shocked gas and its X-ray and IR emissions. A measure of this connection is given by IRX, the IR-to-X-ray flux ratio in the dusty plasma (Dwek 1987).

Many factors determine the value of IRX: the gas density and temperature, which determine the collisional heating rate of the dust and the free–free emission from the gas; the dust-to-gas mass ratio, which determines the relative efficiency of dust and atomic processes in the cooling of the shocked gas; and the grain size distribution which, for a given dust-to-gas mass ratio, determines the efficiency in which the grains absorb the energy of the incident electrons (Dwek 1987; Dwek et al. 2010; Koo et al. 2016).

At sufficiently high electron temperatures or sufficiently small grain radii, electrons penetrate the grains and the dust temperature becomes independent of plasma temperature, and a good diagnostic of gas density. On the other hand, for sufficiently low gas temperatures or large grain radii the electrons are stopped in the grains and the dust temperature provides a strong constraint on the plasma temperature and density.

Models of the X-ray emission from the ring (Ravi et al. 2021) suggest that X-ray emission comprises of a soft X-ray emitting component, generated by a ∼10^3 km s^{-1} shock propagating through the dense clumps of the ring, and a hard X-ray emitting component, generated by the shock propagating through the lower density inter-clump region and the less dense medium in which the ring is embedded. The soft X-ray component is characterized by a temperature of about 0.8 keV ($T_e \approx 10^7$ K), which is consistent with that behind a transmitted 680 km s^{-1} shock through the clumps (Larsson et al. 2019). Using optical spectra of the ring, Mattila et al. (2010) derived preshock densities between ∼(1 and 30) × 10^3 cm^{-3} by fitting emission line light curves with photoionization models. These plasma densities and temperature are capable of collisionally heating the silicate dust grains in the ring to the observed temperature of warm ∼180 K (fig. 6 of Dwek et al. 2010). However, densities above 2 × 10^4 cm^{-3} are required to collisionally heat the secondary hot dust component to temperatures of ∼400–500 K.

For the temperatures inferred from the X-ray observations, most electrons are stopped in the grains. The electron density required to heat the silicate grains to the observed temperature of 180 K is then linearly proportional to the grain and for a fixed electron temperature is approximately given by $n_e(\text{cm}^{-3}) \approx (4 \pm 2) \times 10^4 \times a$, where a is the grain size in μm (fig. 6 of Dwek et al. 2010).

The dust is also destroyed by collisions with the nuclei in the hot plasma. The thermo-kinetic sputtering of the dust is dominated by collisions with H and He nuclei. In a gas that is shocked to temperatures between (1–10)× 10^6 K, the lifetime of silicate dust (t_d) is about $t_d(yrs) = (0.5 - 1.0) \times 10^6 a(\mu m)/n_{ion}(\text{cm}^{-3})$, where n_{ion} is ion density in cm^{-3} (Dwek et al. 1996; Nozawa, Kozasa & Habe 2006). Given the constraint imposed by the dust temperature on the relation between dust radius and gas density, and the uncertainties in the relations, we estimate that the dust lifetime in the shocked ring is between 8 and 32 yrs.

The lifetime of the dust is comparable to the age of the shocked gas. Depending on the details of the shock parameters, a steady supply of dust is needed to sustain the observed IR emission over time. A steady supply of dust is guaranteed as long as the shock expands into the ring. However, eventually, the shocks passes through the ring (Kangas et al. 2021), halting the supply of new dust grains, and depending on the dust lifetime, and plasma cooling time the IR emission from the ER will decline with time (Arendt et al. 2016, 2020).

The IRX remained fairly constant at a value of 2.6 ± 0.5 until day ∼8000, where IR brightness was mainly monitored by *Spitzer* (Dwek et al. 2010). After its helium coolant was exhausted, *Spitzer* monitoring continued only at 3.6 and 4.5 μm, without covering the peak of the IR SED. Nevertheless, after day ∼8000, the fluxes at these two bands plateaued, and then started decreasing at about day 9 000 (Arendt et al. 2016). In contrast, the X-ray brightness at 0.5–2.0 keV continued to increase (Arendt et al. 2016; Frank et al. 2016). The existing *Spitzer* monitoring suggests that the IR/X-ratio seems to decrease after day 9000.

We evaluate the total IR brightness from our mid-IR SEDs, and test if indeed the IRX has changed after day 9000. The IR flux densities between 3.5 and 40 μm from the case 2 SED fits (Section 3.3) result in fluxes of (1.62 ± 0.02) × 10^{-11} erg s^{-1} cm^{-2} and (1.57 ± 0.07) × 10^{-11} erg s^{-1} cm^{-2} at day ∼7954 and day>10 000, respectively. There is little change over the time within the uncertainties. This is more or less consistent with the light curve analysis in Fig. 8, when taking into account the uncertainties in the fluxes.

In contrast, the X-ray brightness at 0.5–2.0 keV continued to increase from (5.6 ± 0.2) × 10^{-12} erg s^{-1} cm^{-2} to (7.9 ± 0.2) × 10^{-12} erg s^{-1} cm^{-2} between day 8000 and 10 433 (Frank et al. 2016). Hence, the IRX decreased from 2.9 ± 0.1 to 2.0 ± 0.1 during this time.

The change in IRX coincides with the time when the brightest part of the ring shifted from the east to the west (Section 3.1.1). We can assume that the IRX of the ring is dominated by the shocks in the east until day ∼7000, and after day 8000, the ratio traces more emission from the west side of the ring.

Determining the causes leading to changes in IRX are complicated, because the degeneracy in many of the physical parameters determining its value. The most fundamental parameter determining IRX is the dust-to-gas mass ratio, which can decease with time because of the effect of grain destruction. The decrease in grains radius due to sputtering can be written as $\Delta a(\mu m) = n_{ion}(\text{cm}^{-3})t(s)/3 \times 10^{13}$, where t is time since the material had been shocked (Dwek et al. 1996; Nozawa et al. 2006). This is proportional to the ionization age $t_{ion} = n_e t$, assuming that $n_e \approx n_{ion}$. An ionization age $t_{ion} \approx 6 \times 10^{11}$ cm^{-3} s was derived from soft X-ray spectra in 2018 (Ravi et al. 2021). This ionization age suggests that grain radii have been decreased by ∼0.02 μm with grains smaller than this being completely destroyed in the shocked gas.

If dust grains are efficiently destroyed in the hot gas, a steady influx of dust into the shocked gas is needed to sustain the observed IR emission. This requires an increase in the volume of shocked gas, which can manifest itself by an increase in the X-ray emission measure (EM) defined as EM = $\int n_p n_e dV$, where n_p is proton density and V is the volume. A two-component model yields a n_e of ∼7500 cm^{-3} for the slow shock and 235 cm^{-3} for the fast shock in earlier days (day 3829; Park et al. 2004). The EM of the soft component increased with time, more than expected by a simply expansion of the disk, until day ∼9000 (Ravi et al. 2021). After that, the EM of the soft component appeared to decrease, while that of the hard component continued to increase, with the rate changing at

about day ~9000. There are two complications in interpreting the EM. First, the shocks exited the ring on the east side around day ~9000, so that the EM does not reflect a simple increasing volume anymore at this point. Secondly, Ravi et al. (2021) mentions that a simple two-component model analysis shows that the soft and hard components are becoming merged, and also the energy from the hard component contributes more to the total energy in post day ~9000. Because this day is coincident with the time when the dominant component shifts from the east to west side of the ring, it might be possible that fundamentally, the properties of shocks on the east and the west are different. It might be possible that the west side of the ring has a higher density, and causing harder shock energy, and also higher n_e. However, with limited angular resolution in X-ray spectra, it is hard to evaluate.

5 CONCLUSIONS

Our MIR images of SN 1987A show that the IR emission is 60 per cent dominated by dust emission from the west side of the circumstellar ring in recent years (2017–2022). That is in contrast to IR images up to 2006, when the east side of the ring dominated the overall IR brightness (nearly 80 per cent). The east side of the ring was hit by the blast waves earlier, causing them to brighten and led to the higher measured dust temperatures in the early 2000s. After the shock waves passed the east side, the IR emission faded on that side. Blast waves reached the west side of the ring later, and now the IR emission is dominated by the west side of the ring. The shift of brightness from the east to the west is consistent with what was observed in the optical and the X-ray images. The MIR observations also confirm that the IR/X-ray brightness ratio has been decreased in recent years. This is mainly due to the increase of X-ray brightness, while the IR brightness has remained more or less constant within the uncertainties.

We suggest that the most likely cause for the decrease in the IR/X-ray ratio is that the west side of the circumstellar ring has different properties from the east. It can be due to higher density, higher electron density, or/and longer ionization time-scale.

In summary, more precise models and more observations spanning a wider range of IR and X-ray wavelengths at higher resolution are required to quantitatively evaluate which effect(s), gas cooling, dust destruction, changes in gas density, or the exhaustion of new shocked gas and dust are responsible for the changes in the relative intensities of the global and local X-ray and IR emissions.

DATA AVAILABILITY

The VISIR data are posted at ESO archive, and the VISIR and GEMINI reduced data will be available on request to the authors.

REFERENCES

Alp D. et al., 2018, ApJ, 864, 174
Arendt R. G., Dwek E., Bouchet P., Danziger I. J., Gehrz R. D., Park S., Woodward C. E., 2020, ApJ, 890, 2
Arendt R. G. et al., 2016, AJ, 151, 62
Arendt R. G., Dwek E., Kober G., Rho J., Hwang U., 2014, ApJ, 786, 55
Barlow M. J. et al., 2010, A&A, 518, L138
Biscaro C., Cherchneff I., 2014, A&A, 564, A25
Biscaro C., Cherchneff I., 2016, A&A, 589, A132
Bouchet P., De Buizer J. M., Suntzeff N. B., Danziger I. J., Hayward T. L., Telesco C. M., Packham C., 2004, ApJ, 611, 394
Bouchet P. et al., 2006, ApJ, 650, 212
Burrows C. J., Kristx J., Hester J. J., 1995, ApJ, 452, 680
Chawner H. et al., 2019, MNRAS, 483, 70
Cigan P. et al., 2019, ApJ, 886, 51
Cohen M., Walker R. G., Carter B., Hammersley P., Kidger M., Noguchi K., 1999, AJ, 117, 1864
De Looze I., Barlow M. J., Swinyard B. M., Rho J., Gomez H. L., Matsuura M., Wesson R., 2017, MNRAS, 465, 3309
Draine B. T., Lee H. M., 1984, ApJ, 285, 89
Dwek E., 1987, ApJ, 322, 812
Dwek E., Arendt R. G., 1992, ARA&A, 30, 11
Dwek E., Cherchneff I., 2011, ApJ, 727, 63
Dwek E., Foster S. M., Vancura O., 1996, ApJ, 457, 244
Dwek E. et al., 2008, ApJ, 676, 1029
Dwek E. et al., 2010, ApJ, 722, 425
Frank K. A., Zhekov S. A., Park S., McCray R. A., Dwek E., Burrows D. N., 2016, ApJ, 829, 40
Fransson C. et al., 2015, ApJ, 806, L19
Freudling W. et al., 2013, A&A, 559, A96
Gomez H. L. et al., 2012, ApJ, 760, 96
Gordon K. D. et al., 2014, ApJ, 797, 85
Herter T. L. et al., 2012, ApJ, 749, L18
Hildebrand R. H., 1983, Q. J. R. Astron. Soc., 24, 267
Indebetouw R. et al., 2014, ApJ, 782, L2

Jones A. P., Tielens A. G. G. M., Hollenbach D. J., 1996, ApJ, 469, 740

Kangas T. et al.., 2022, MNRAS, 511, 2977

Käufl H. U. et al.., 2015, Messenger, 159, 15

Kirchschlager F., Mattsson L., Gent F. A., 2021, MNRAS, 509, 3218

Kirchschlager F., Schmidt F. D., Barlow M. J., Fogerty E. L., Bevan A., Priestley F. D., 2019, MNRAS, 489, 4465

Koo B.-C. C., Lee J.-J., Jeong I.-G., Seok J. Y., Kim H.-J., 2016, ApJ, 821, 1

Lagage P. O. et al.., 2004, Messenger, 117, 12

Larsson J. et al., 2016, ApJ, 833, 147

Larsson J. et al., 2019, ApJ, 886, 147

Li D., Telesco C. M., Varosi F., 2010, in Proc. SPIE Conf. Ser. Vol. 7737, Observatory Operations: Strategies, Processes, and Systems, Characterization of the mid-IR image quality at Gemini South. SPIE, Bellingham, p. 77372F

McCray R. A., 1993, ARA&A, 31, 175

McCray R. A., Fransson C., 2016, ARA&A, 54, 19

Markwardt C. B., 2009, in Bohlender D. A., Durand D., Dowler P., eds, ASP Conf. Ser. Vol. 411., Astronomical Data Analysis Software and Systems XVIII, Non-linear Least-squares Fitting in IDL with MPFIT. Astron. Soc. Pac., San Francisco, p. 251

Matsuura M. et al., 2018, MNRAS, 482, 1715

Matsuura M. et al., 2015, ApJ, 800, 50

Matsuura M. et al., 2011, Science, 333, 1258

Mattila S., Lundqvist P., Groningsson P., Meikle W. P. S., Stathakis R., Fransson C., Cannon R., 2010, ApJ, 717, 1140

Micelotta E. R., Dwek E., Slavin J. D., 2016, A&A, 590, A65

Morris T., Podsiadlowski P., 2007, Science, 315, 1103

Ng C.-Y., Zanardo G., Potter T. M., Staveley-Smith L., Gaensler B. M., Manchester R. N., Tzioumis A. K., 2013, ApJ, 777, 131

Nozawa T., Kozasa T., Habe A., 2006, ApJ, 648, 435

Nozawa T., Kozasa T., Habe A., Dwek E., Umeda H., Tominaga N., Maeda K., Nomoto K., 2007, ApJ, 666, 955

Page D., Beznogov M. V., Garibay I., Lattimer J. M., Prakash M., Janka H.-T., 2020, ApJ, 898, 125

Panagia N., Scuderi S., Gilmozzi R., Challis P. M., Garnavich P. M., Kirshner R. P., 1996, ApJ, 459, L17

Park S., Zhekov S. A., Burrows D. N., Garmire G. P., McCray R., 2004, ApJ, 610, 275

Press W. H., Flannery B. P., Teukolsky S. A., Vetterling W. T., 1989, Numerical Recipes in C. The Art of Scientific Computing. Cambridge Univ. Press, Cambridge

Priestley F. D., Chawner H., of M. M., 2021, MNRAS, 500, 2543

Ravi A. P., Park S., Zhekov S. A., Miceli M., Orlando S., Frank K. A., Burrows D. N., 2021, ApJ, 922, 140

Reunanen J., Prieto M. A., Siebenmorgen R., 2010, MNRAS, 402, 879

Rybicki G. B., Lightman A. P., 1986, Radiative Processes in Astrophysics. Wiley-VCH Verlag, Weinheim

Sarangi A., Cherchneff I., 2013, ApJ, 776, 107

Sarangi A., Cherchneff I., 2015, A&A, 575, A95

Sarangi A., Matsuura M., Micelotta E. R., 2019, in Bykov A., Roger C., Raymond J., Thielemann F.-K., Falanga M., von Steiger R., eds, Vol. 68, Supernovae. Series: Space Sciences Series of ISSI. Springer, p. 313

Schneider R., Ferrara A., Salvaterra R., 2004, MNRAS, 351, 1379

Silvia D. W., Smith B. D., Shull J. M., 2010, ApJ, 715, 1575

Slavin J. D., Dwek E., Jones A. P., 2015, ApJ, 803, 7

Slavin J. D., Dwek E., Low M.-M. M., Hill A. S., 2020, ApJ, 902, 135

Sluder A., Milosavljević M., Montgomery M. H., 2018, MNRAS, 480, 5580

Spitzer L., 1978, Physical Processes in the Interstellar Medium. A Wiley-Interscience Publication, New York

Weingartner J. C., Draine B. T., 2001, ApJ, 548, 296

Young E. T. et al., 2012, in Proc. SPIE Conf. Ser. Vol. 8444, Ground-based and Airborne Telescopes IV, Early Science Results from SOFIA. SPIE, Bellingham, p. 844410

Zanardo G. et al., 2014, ApJ, 796, 82

Zanardo G., Staveley-Smith L., Ng C.-Y., Gaensler B. M., Potter T. M., Manchester R. N., Tzioumis A. K., 2013, ApJ, 767, 98

Zubko V. G., Mennella V., Colangeli L., Bussoletti E., 1996, MNRAS, 282, 1321

This paper has been typeset from a TEX/LATEX file prepared by the author.